Electronic Supplementary Material (ESI) for Physical Chemistry Chemical Physics.

Electronic Supplementary Information

Adhesion and friction behaviors of γ-Fe/diamond heterogeneous contact interface: A density functional theory study

Qizhen He[a], Lixiang Rao[a*], Wenwei Song[a], Hailiang Liu[a], Silong Zhang[a] Xuejun Ren[b] and Qingxiang Yang[a*]

[a] State Key Laboratory of Metastable Materials Science & Technology, Hebei key lab for optimizing metal product technology and performance, College of Materials Science & Engineering, Yanshan University, Qinhuangdao 066004, PR China

[b] School of Engineering, Liverpool John Moores University, Liverpool L3 3AF, UK

* Corresponding author: Tel. **+86-335-838-7471**, Fax. **+86-335-807-4545**

E-mail address: qxyang@ysu.edu.cn, **1310454098 @qq.com**

Section I Convergence test of plane-wave cutoff and k-point mesh

Convergence test of plane-wave cutoff and k-point mesh were performed to ensure the accuracy of the calculation as shown in **Fig. S1**. From **Fig. S1**, the plane-wave cutoff used for bulk, surface and interface calculation can be set as 400 eV. K-point mesh of 7×7×7, 5×5×5 was used for calculations of bulk Fe and diamond, respectively. K-point mesh of 7×7×1, 5×5×1 was used for calculations of Fe and diamond surface, respectively. k-point mesh of 7×7×1 was used for all interfaces.

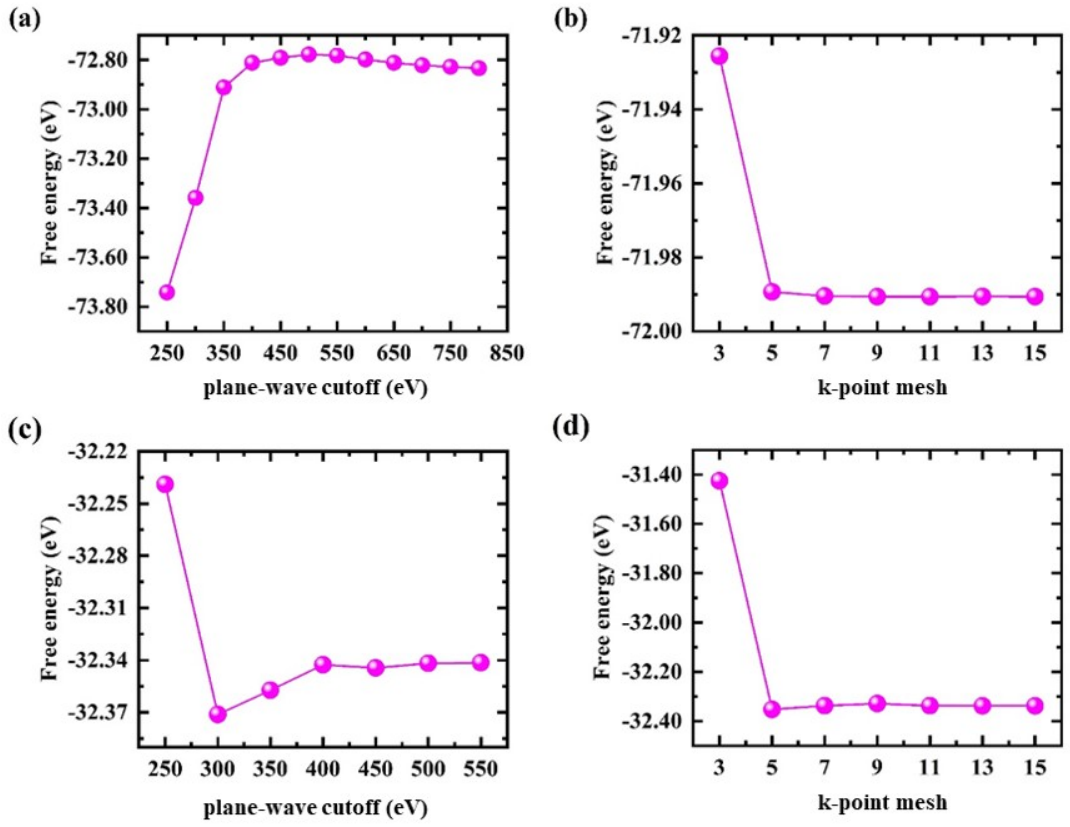

Fig. S1 Convergence test of plane-wave cutoff and k-point mesh for diamond and Fe. (a) and (b) are convergence test of plane-wave cutoff and k-point mesh for diamond, respectively. (c) and (d) are those for Fe.

Section II Structural stability of bulk diamond and γ-Fe

Fig. S2 shows that bulk structures of diamond and γ-Fe. From **Fig. S2 (a)**, the diamond crystal can be described as two inter-penetrating face-centered-cubic (FCC) structures with relative shifting of $\frac{1}{4}[111]$, which belongs to the space group Fd-3m (227). The lattice constant after relaxation is a = 3.574 Å, which is basically consistent with the experimental value (a = 3.567 Å) in ref. **[1]** and the simulated value (a = 3.577 Å) in ref. **[2]**. From **Fig. S2 (b)**, γ-Fe with the face centered cubic structure is used in this work, which belongs to the space group Fm-3m. The relaxed lattice constant is a = 3.637 Å, which is basically consistent with the measured value (a = 3.645 Å) in ref. **[3]** and the calculated value (a = 3.474 Å) in ref. **[4]**.

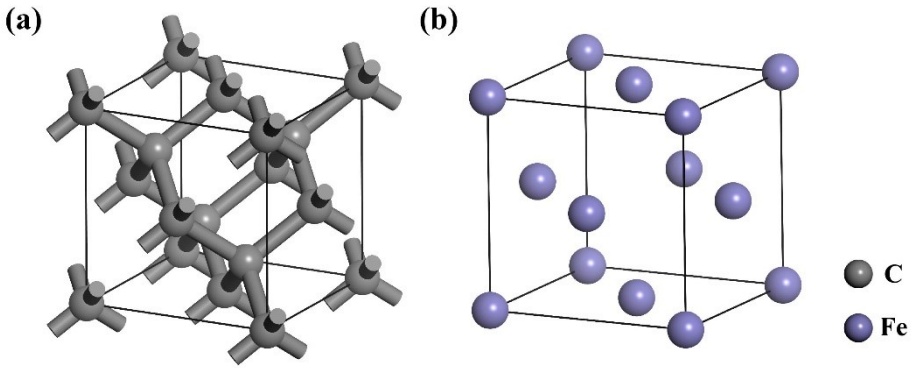

Fig. S2 Bulk structures of (a) diamond and (b) γ-Fe.

In order to verify the dynamic stability of diamond and Fe structures used and reflect their bonding strength, the VASP with the PHONOPY package was applied to calculate the phonon dispersion curves and the harmonic second-order interatomic force constants (*IFC*) by the density functional perturbation theory (DFPT) method for 2×2×2 supercell. The *IFC* tensor is defined as follow:

$$\frac{\partial^2 E}{\partial R_i \partial R_j} = \begin{bmatrix} \frac{\partial^2 E}{\partial R_x \partial R_x} & \frac{\partial^2 E}{\partial R_x \partial R_y} & \frac{\partial^2 E}{\partial R_x \partial R_z} \\ \frac{\partial^2 E}{\partial R_y \partial R_x} & \frac{\partial^2 E}{\partial R_y \partial R_y} & \frac{\partial^2 E}{\partial R_y \partial R_z} \\ \frac{\partial^2 E}{\partial R_z \partial R_x} & \frac{\partial^2 E}{\partial R_z \partial R_y} & \frac{\partial^2 E}{\partial R_z \partial R_z} \end{bmatrix} \tag{1}$$

where E and R are the potential energy and atomic displacement, respectively.

The traces of *IFC* tensors between one atom chosen as the origin and another atom was normalized by the trace of the self-interaction *IFC* tensor of the origin atom. Related formula **[5]** are as follows:

$$trace\ of\ IFC = \frac{\partial^2 E}{\partial R_x \partial R_x} + \frac{\partial^2 E}{\partial R_y \partial R_y} + \frac{\partial^2 E}{\partial R_z \partial R_z} \tag{2}$$

$$Normalized\ Trace\ of\ IFC = \frac{\frac{\partial^2 E}{\partial R_{0,x} \partial R_{n,x}} + \frac{\partial^2 E}{\partial R_{0,y} \partial R_{n,y}} + \frac{\partial^2 E}{\partial R_{0,z} \partial R_{n,z}}}{\frac{\partial^2 E}{\partial R_{0,x} \partial R_{0,x}} + \frac{\partial^2 E}{\partial R_{0,y} \partial R_{0,y}} + \frac{\partial^2 E}{\partial R_{0,z} \partial R_{0,z}}} \tag{3}$$

where R_0 and R_n denotes the displacement of the origin atom and the n-th neighbor atom, respectively.

Phonon dispersion curves of diamond and γ-Fe and their normalized trace of *IFC* versus atomic distances are shown in **Fig. S3**. From **Fig. S3 (a)** and **(b)**, there is no imaginary frequency modes in the Brillouin zone for diamond and γ-Fe we used, which indicates that diamond and γ-Fe are all dynamically stable. **Fig. S3 (c)** shows the bonding state between the central atom and its neighboring atoms in diamond and Fe structures. From **Fig. S3 (c)**, for diamond structure, it is obvious that an anomalous nonmonotonic trend of the *IFC*s, which indicates that the monotonic decay of interaction strength versus distance. While for γ-Fe structure, large long-range interactions are present at specific neighboring shells, e.g. the second and fourth nearest

neighbor. In addition, fifth-nearest neighbors have even positive force constants, giving them the behavior of "anti-springs".

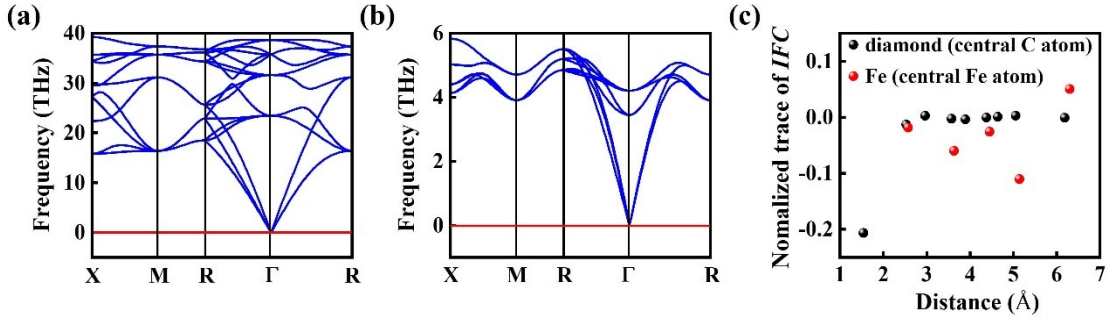

Fig. S3 Phonon dispersion curves of diamond and γ-Fe and their normalized trace of *IFC* versus atomic distances. (a) and (b) are phonon dispersion curves of diamond and γ-Fe, respectively. (c) is their normalized trace of *IFC* versus atomic distances. The element in the parenthesis indicates the interaction between the corresponding atom and other atoms in (c).

Section III Electronic structure of diamond and Fe

The electron localization function (ELF) **[6-8]** essentially is an indicator of measuring electron localization degree in local region, which is applied to reflect electronic localized states of diamond and Fe structures. It can be defined as follows:

$$ELF(r) = \frac{1}{1+[D(r)/D_0(r)]^2} \tag{4}$$

$$D(r) = \frac{1}{2}\sum_i \eta_i |\nabla\varphi_i(r)|^2 - \frac{1}{8}\frac{|\nabla\rho(r)|^2}{\rho(r)},\ D_0(r) = (3/10)(3\pi^2)^{2/3}\rho(r)^{5/3} \tag{5}$$

where φ and η denote orbital wavefunction and orbital occupation number, respectively; ρ corresponds to electron density, r is position vector. ELF is a uniquely defined dimensionless quantity, and only takes values in the range between 0 and 1, where 1 refers to the fully localized electrons, and 0.5 corresponds to fully delocalized electrons, while 0 represents very low charge density.

Fig. S4 shows that electron localization function (ELF) for diamond and γ-Fe. A strong electron localization is found in diamond structure (as shown in **Fig. S4 (a)** and

(c)), which indicates that diamond is a covalent material with strong bonding. While, there is basically no electron localization in Fe structure (see **Fig. S4 (b)** and **(d)**), which shows that γ-Fe is a material with weak metal bond.

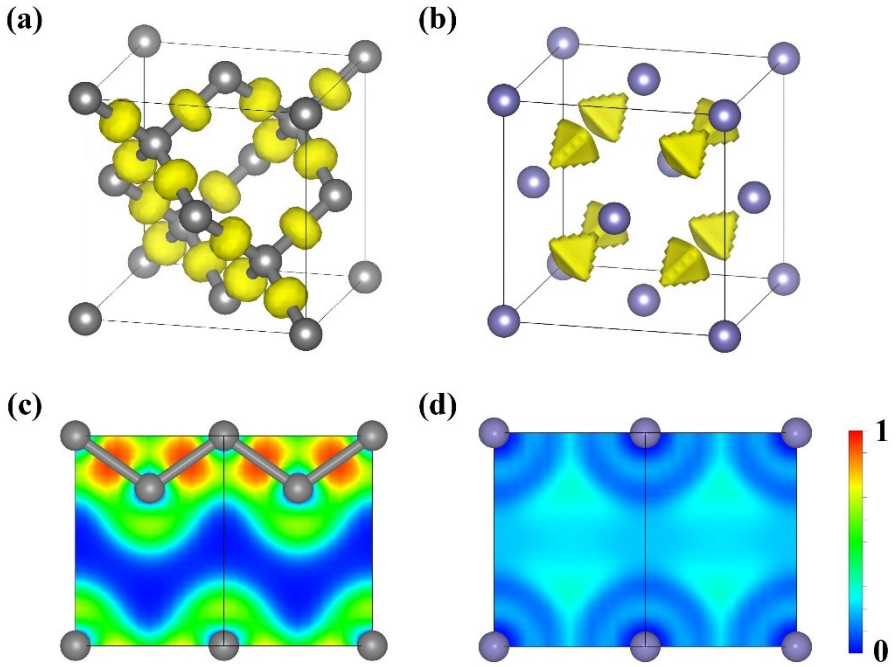

Fig. S4 Electron localization function (ELF) for diamond and γ-Fe. (a) and (b) are iso-surface at ELF levels of 0.85 and 0.18 for diamond and γ-Fe, respectively. (c) and (d) are 2D slices (correspond (110) plane) for diamond and γ-Fe, respectively.

Fig. S5 shows electronic band structures along the high symmetry directions in the first Brillouin zone and Fermi surfaces of diamond and γ-Fe. Diamond is an insulator with direct band gap of 4.58 eV, which is basically consistent with the measured value (5.55 eV) in ref. **[9]** and the calculated value (4.15 eV) in ref. **[10]** as shown in **Fig. S5 (a)**. For the band structures of γ-Fe structure as shown in **Fig. S5 (b)** and **(c)**, it is obvious that the valence bands pass through the Fermi level (E_F) and overlap the conduction bands, which suggests an electron-conducting behavior. Fermi surfaces as shown in **Fig. S5 (c)** and **(d)** are also investigated to facilitate the understanding of the physical properties of γ-Fe structure, which is called ‘‘the face of

metal'' **[11]** and strongly affects the properties of metals because it is the most active region in reciprocal space. The Fermi level is the boundary between the occupied state and the unoccupied state of the electron. In the three-dimensional reciprocal space, the Fermi level is the surface of the energy E_F in the K space **[12]**. Fermi surface is drawn by software FermiSurfer **[13]**. From **Fig. S5 (c)** and **(d)**, it can be found that the Fermi surface was compatible with a tight-binding energy band for γ-Fe lattice, which is with the characteristic of Fermi surface for fcc metal.

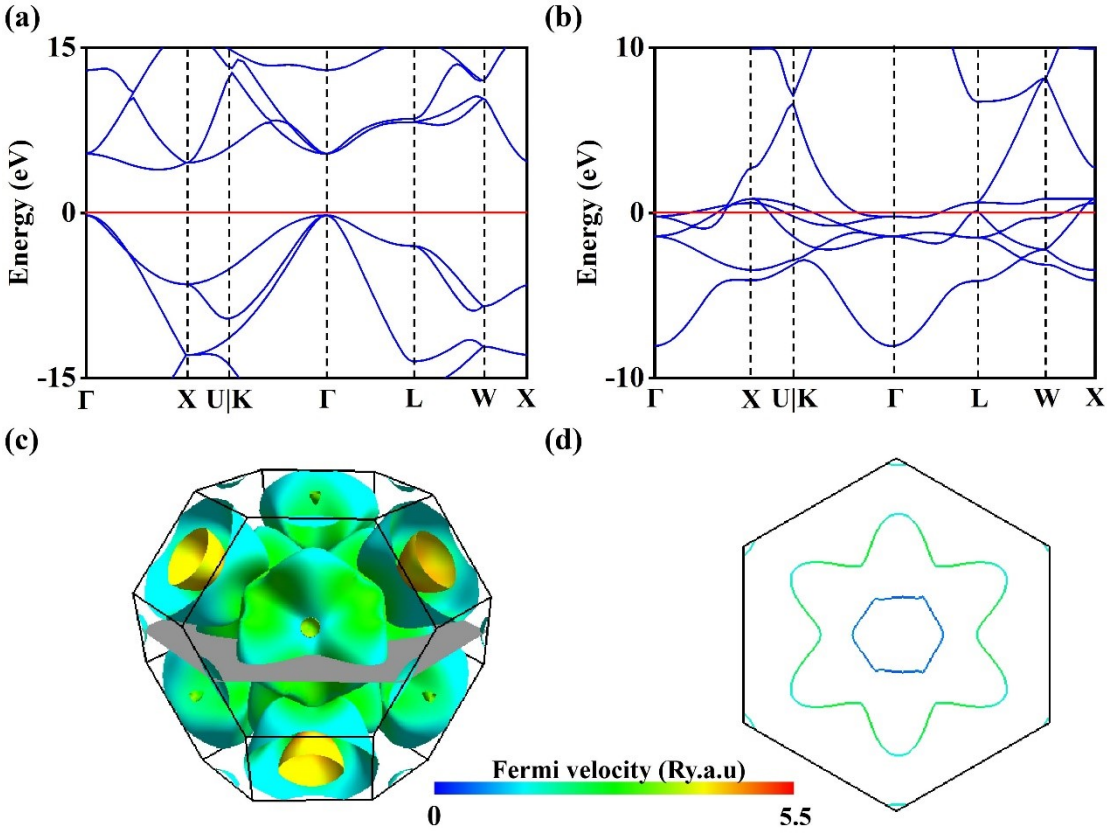

Fig. S5 Electronic band structures and Fermi surfaces of diamond and γ-Fe. (a) and (b) are electronic band structure of diamond and γ-Fe. (c) and (d) are Fermi surface and corresponding section of γ-Fe, respectively. the Fermi energy is set as zero point (0.0 eV).

Section IV Electronic property of diamond and Fe surface

The work function is defined as the minimum amount of energy required to move an electron from the interior of the solid to vacuum far away from the surface of materials, which can reflect the strength of the electron binding ability. Work function Φ **[34**, **35]** is defined as follows:

$$\Phi = E_{\text{vac}} - E_F \tag{18}$$

where E_{vac} is the energy of a stationary electron in the vacuum nearby the surface. E_{F} determines the ground state electronic structure calculation. Calculated work functions for diamond and Fe surfaces are shown in **Fig. S6**. From **Fig. S6**, work functions of all diamond surfaces are larger than those of γ-Fe surfaces. Meanwhile, it is worth noting that work functions of low-index surfaces for diamond and Fe are different, which exhibits anisotropy of the work function for diamond and γ-Fe. What is more, it should be pointed out that our calculated results for diamond and γ-Fe are in good agreement with those in other literatures **[36-39]**.

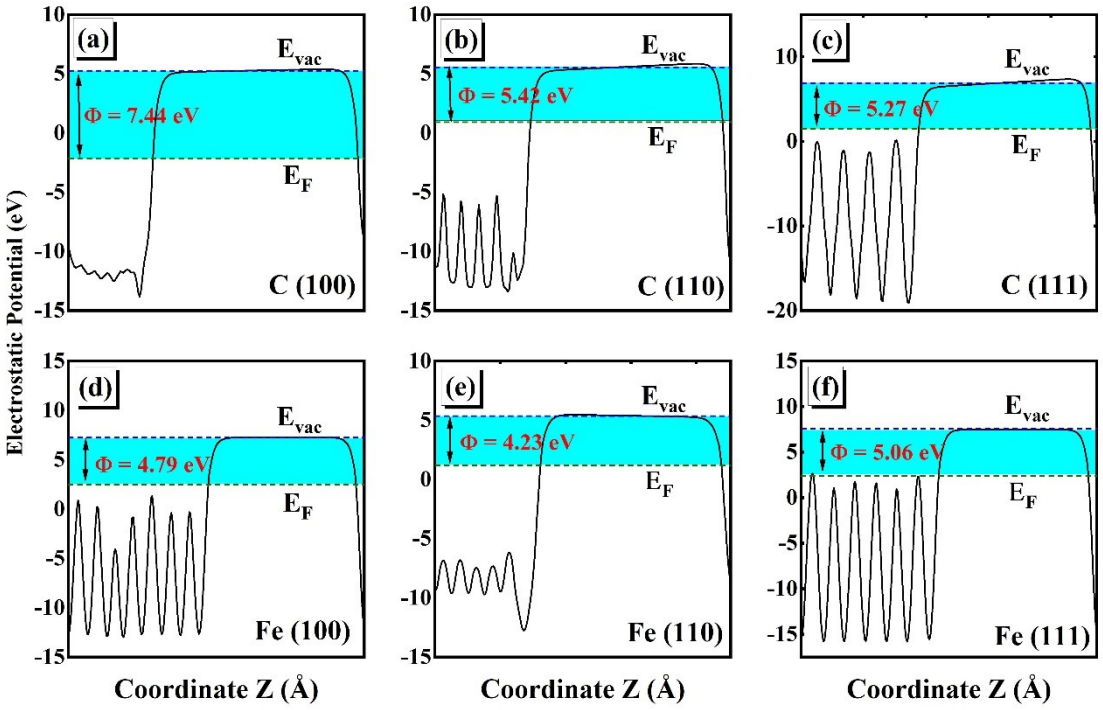

Fig. S6 Calculated work functions for diamond and γ-Fe surfaces. (a), (b) and (c) are calculated work functions of (100), (110) and (111) surfaces for diamond, respectively. (d), (e) and (f) are those for Fe. The green and blue dashed lines denote Fermi level and the vacuum energy level, respectively.

Section V Mechanical property of bulk diamond and Fe

The elastic properties were calculated using energy-strain method **[14**, **15]**. The internal energy of a crystal under strain ε can be represented by Taylor expansion in power of the strain tensor. Related equation is as follows:

$$E(V,\{\varepsilon_i\}) = E(V_0\,0) + V_0\sum_{i}^{6}\sigma_i\varepsilon_i + \frac{V_0}{2}\sum_{i,j=1}^{6}c_{ij}\varepsilon_i\varepsilon_j + \cdots, \tag{6}$$

where $E(V_0,0)$ and V_0 are the energy and volume of the reference structure (usually the equilibrium one), respectively.

For diamond and Fe structures, which belongs to cubic system, there are only three independent elastic constants (i.e. C_{11}, C_{12} and C_{44}). The three Born stability criteria **[16]** for the cubic system are adopted to verify the mechanical stability of the C-

Nonmetal models. The related criteria are as follows:

$$C_{11} - C_{12} > 0,\ C_{11} + 2C_{12} > 0,\ C_{44} > 0 \tag{7}$$

Meanwhile, the Voigt-Reuss-Hill approximations **[17-19]** were also used to calculate the elastic modulus of diamond and γ-Fe including bulk modulus (*B*), shear modulus (*G*), Young's modulus (*E*) and Poisson's ratio (*v*). The relevant equations are given in equation (4)-(8). In cubic crystal, there are only 3 independent variables as equation (9).

$$B = \frac{B_V + B_R}{2}, G = \frac{G_V + G_R}{2}, E = \frac{9BG}{3B + G}, \nu = \frac{3B - E}{6B} \tag{8}$$

$$B_V = [(C_{11} + C_{22} + C_{33}) + 2(C_{12} + C_{13} + C_{23})] / 9 \tag{9}$$

$$B_R = 1 / [(S_{11} + S_{22} + S_{33}) + 2(S_{12} + S_{13} + S_{23})] \tag{10}$$

$$G_V = [(C_{11} + C_{22} + C_{33} - C_{12} - C_{13} - C_{23}) + 3(C_{44} + C_{55} + C_{66})] / 15 \tag{11}$$

$$G_R = 15 / [4(S_{11} + S_{22} + S_{33} - S_{12} - S_{13} - S_{23}) + 3(S_{44} + S_{55} + S_{66})] \tag{12}$$

$$C_{11} = C_{22} = C_{33},\ C_{12} = C_{13} = C_{23},\ C_{44} = C_{55} = C_{66} \tag{13}$$

The elastic constants of diamond and γ-Fe meet the three Born stability criteria, whose detailed data are listed in **Table S1**, which indicates that there is mechanical stability for diamond and γ-Fe structures. Meanwhile, our calculated results are in good agreement with the experimental and other theoretical values **[20-23]** for diamond structure. It is worth noting that calculated results for Fe are closer to the experimental results than other calculated values **[24-27]**. In addition, it is obvious that the *B*, *G* and *E* of diamond are all larger than those of Fe. While, the *v* of γ-Fe is higher than that of diamond, which shows that the transverse deformation ability of γ-Fe is stronger than that of diamond. In order to quantitatively compare the brittleness of diamond and γ-Fe,

the ratio of the shear modulus to the bulk modulus, i.e. Pugh ratio (G/B) **[28]** was calculated. In generally, if $G/B < 0.57$, the material is ductile, otherwise, the material behaves in a brittle. It is worth noting that the larger G/B is, the more brittleness of the material is. Pugh ratio of diamond is 1.195 (>0.57) and that of Fe is 0.741 (>0.57), which suggests that diamond and γ--Fe structures we used are all brittle materials while the brittleness of diamond is much higher than that of γ-Fe.

Table S1 Comparison of experimental and theoretical second order elastic constants of diamond and γ-Fe

System	C_{11}/GPa	C_{12}/GPa	C_{44}/GPa	B/GPa	G/GPa	E/GPa	υ
diamond							
This work	1050.21	125.32	559.35	433.62	518.34	1111.95	0.07
Theory[a]	1053	125	560	434.33	519.40	1114.10	0.07
Theory[a]	1105.6	149.4	592.6	468.13	543.80	1176.02	0.08
Theory[b]	1054	124	559	432.00	519.29	1113.69	0.07
Exper.[c]	1080.4	127.0	5342	444.80	510.47	1107.68	0.08
Exper.[d]	1079.26	126.73	578.16	444.24	534.99	1141.56	0.07
fcc-Fe							
This work	260.56	99.03	142.20	152.87	113.32	272.61	0.20
Theory[e]	540	120	260	260	239.7	548.30	0.15
Exper.[f]	154	143.9	78.4	147.27	31.79	88.96	0.40
Exper.[g]	181	156	83.3	164.33	40.24	111.62	0.39
Exper.[h]	154	122	77	132.67	41.55	112.86	0.36

[a] Ref**[20]**, [b] Ref**[21]**, [c] Ref**[22]**, [d] Ref**[23]**, [e] Ref**[24]**, [f] Ref**[25]**, [g] Ref**[26]**, [h] Ref**[27]**

Two different models (Chen's model and Tian's model) were employed to reflect the intrinsic hardness H_V of diamond and γ-Fe structure. The related expressions **[29-30]** are as follows:

$$H_V^{Chen} = 2(k^{-2}G)^{0.585} - 3 \quad (14)$$

$$H_V^{Tian} = 0.92k^{-1.137}G^{0.708} \quad (15)$$

where k is equal to B/G. The H_V^{Chen} and H_V^{Tian} of diamond are 92.45 and 94.16 GPa while those of γ-Fe are 19.42 and 18.64 GPa, which shows that the hardness of diamond is much larger than that of Fe.

Based on the obtained elastic constants, key quantities (Young's modulus (E), Linear compressibility (LC), Shear modulus (G) and Poisson's ratio (υ) as shown in **Fig. S7**) were investigated to characterize the mechanical behavior of the crystal in the elastic range. It is worth mentioning that Young's modulus and Linear compressibility (LC) are functions of a single unit vector ***a***: $E(\boldsymbol{a})$ and $LC(\boldsymbol{a})$ and ***a*** is fully characterized by the angles θ (0, π) and φ (0, 2π). However, the shear modulus G and Poisson's ratio υ are not as straightforward to represent, because they depend on two orthogonal unit vectors ***a*** and ***b*** (respectively the direction of the stress applied and the direction of measurement). Herein, another unit vector ***b*** is defined, which is perpendicular to the first unit vector ***a*** and characterized by the angle χ (0, 2π). Detailed diagram and definitions of angles used to describe directions are shown in **Fig. S8**. The coordinates of the two vectors ***a*** and ***b*** **[31]** are defined as:

$$\boldsymbol{a} = \begin{pmatrix} \sin(\theta)\cos(\varphi) \\ \sin(\theta)\sin(\varphi) \\ \cos(\theta) \end{pmatrix} \text{ and } \boldsymbol{b} = \begin{pmatrix} \cos(\theta)\cos(\varphi)\cos(\chi) - \sin(\varphi)\sin(\chi) \\ \cos(\theta)\sin(\varphi)\cos(\chi) + \cos(\varphi)\sin(\chi) \\ -\sin(\theta)\cos(\chi) \end{pmatrix} \quad (16)$$

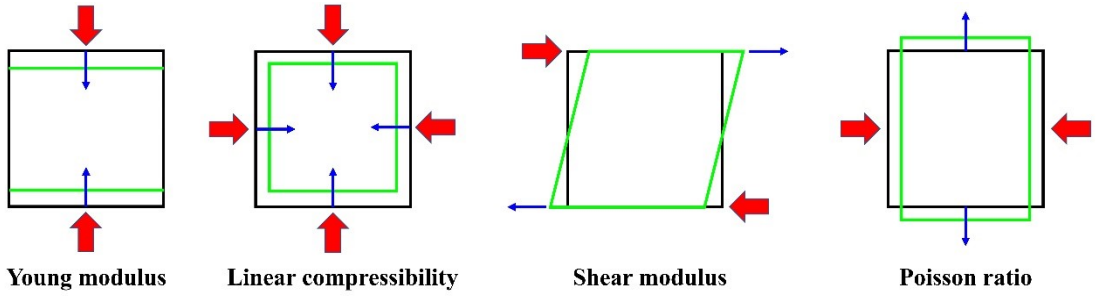

Fig. S7 Scheme of the directional elastic properties calculated in this work. For each, large red arrows represent the direction of applied stress and smaller blue arrows the direction along which the resulting strain is measured.

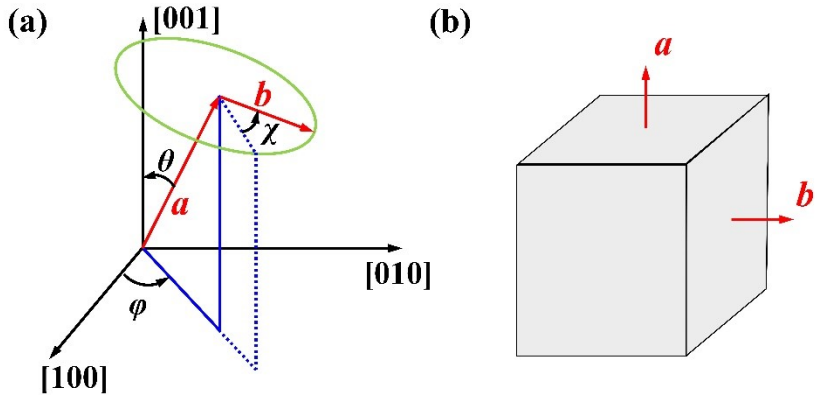

Fig. S8 Definitions of angles used to describe directions. (a) is definition of primary and secondary orientations in crystal coordinate system. (b) is the relation between orientations and specimen geometry. ***a***, ***b***, θ, φ, χ are the unit vector along primary orientation, the unit vector along secondary orientation, the polar angle (φ), the azimuth angle and the angle between ***b*** and line projected from ***a*** on horizontal plane then projected on the plane normal to ***a***.

Fig. S9 shows that spatial dependence of Young's modulus (E), Linear compressibility (LC), Shear modulus (G) and Poisson's ratio (υ) for bulk diamond and γ-Fe. A higher degree of isotropic elastic properties results in the smaller variation in the magnitude of the three-dimensional (3D) surfaces and 2D contours. The 2D projection plots correspond to a cut through the 3D surface plots on the XY, XZ, and YZ planes. The maximum-to-minimum Young's modulus ratio for diamond and γ-Fe is 1.15 and 1.58, respectively, which shows that diamond is with little anisotropy characteristic and there is no negligible one for γ-Fe structure. Meanwhile, for diamond structure, the maximum value of 1173.5 GPa corresponds to the <111> direction while the minimum value for the <100> direction is 1023.5 GPa (see **Fig. S9 (a)** and **(a1)**). For γ-Fe structure used, the maximum and minimum values of 325.6 and 206.0 GPa correspond to the <111> and <100> direction (see **Fig. S9(e)** and **(e1)**), respectively. The 3D surface plot for the linear compressibility of diamond and Fe structures is an approximate sphere, which shows negligible anisotropy for diamond and Fe structures because their values of linear compressibility are 0.76 and 0.77 TPa^{-1} in all directions

(see **Fig. S9 (b)**, **(b1)**, **(f)** and **(f1)**), respectively. The range of the minimum and maximum values of the shear modulus and Poisson's ratios for each direction of the applied stress is attributed to the variation in the direction of the measurement, which is the change of angle χ. In the 3D surface plots of the shear modulus and Poisson's ratio, the translucent blue surface represents the maximal values and envelops the solid green surface inside, which represents the minimal values. The minimum surface has a color map applied such that darker colors represent smaller values than brighter colors as shown in **Fig. S9 (c)**, **(d)**, **(g)** and **(h)**. In the 2D plots, the maximum values are represented by a blue curve, and the minimum values are denoted by a green curve as shown in **Fig. S9 (c1)**, **(d1)**, **(g1)** and **(h1)**. For diamond structure, the ratio of the maximum to the minimum shear modulus values is 1.17, and the maximum and minimum values are 559.35 GPa in the <100> direction and 462.45 GPa in the <111> directions (see **Fig. S9 (c)** and **(c1)**), respectively. Furthermore, the ratio of the maximum Poisson's ratio to the minimum one is 9.92. The maximum and minimum values occur in the <110> direction with value of 0.44 and <111> direction with value of 0.33 (see **Fig. S9 (d)** and **(d1)**), respectively. For γ-Fe structure, the ratio of maximum to minimum shear modulus values is 1.76 and the maximum value (142.19 GPa) and minimum one (80.77 GPa) are in <100> and <111> directions as shown in Fig. 6 (g) and (g1), respectively. In addition, the maximum and minimum Poisson's ratio values are both occur in <110> direction as shown in **Fig. S9 (h)** and **(h1)**, which are 0.38 and 0, respectively. The universal anisotropy index (A^{U}) also is calculated to evaluate the anisotropy of diamond and γ-Fe structures, which can generally be applied

to crystal systems that consider the bulk component of the elastic tensor **[32]**. Related equation is as follows:

$$A^{U} = 5\frac{G_V}{G_R} + \frac{B_V}{B_R} - 6 \geq 0 \tag{17}$$

Based on the above equation, the A^{U} values of diamond and γ-Fe structures are 0.04 and 0.39, which indicates that the anisotropy of γ-Fe is slightly stronger than that of diamond.

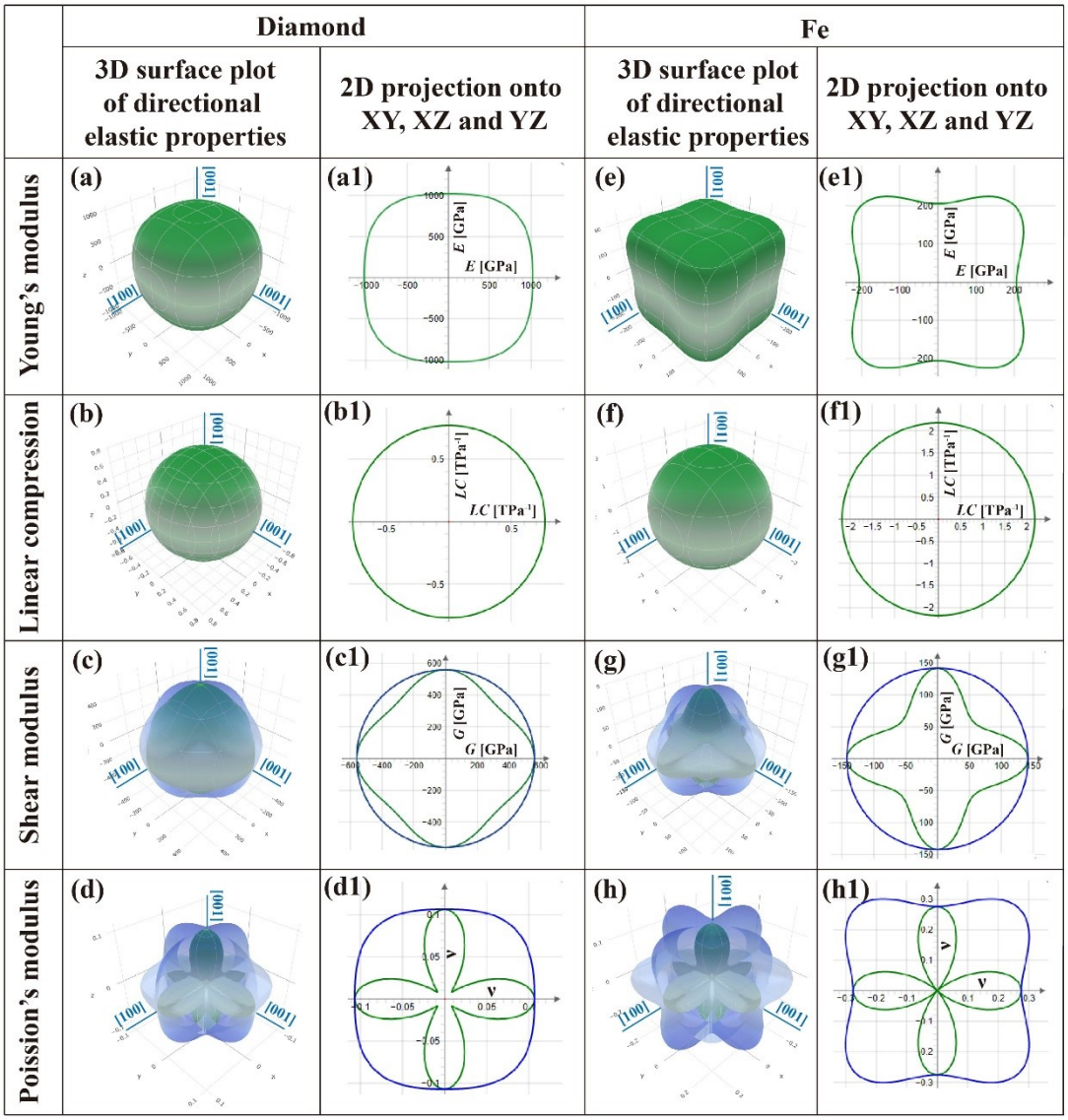

Fig. S9 Spatial dependence of Young's modulus, Linear compressibility, Shear modulus and Poisson's ratio for bulk diamond and γ-Fe. (a), (b), (c) and (d) are 3D surface plot of Young's modulus, Linear compressibility, Shear modulus and Poisson's ratio for bulk diamond, respectively.

(a1), (b1), (c1) and (d1) are corresponding 2D projection onto XY, XZ and YZ, respectively. Similarly, (e)-(h) and (e1)-(h1) are those 3D surface plot and 2D projection onto XY, XZ and YZ for γ-Fe, respectively.

In our prior work **[33]**, rotating lattice matrix and the calculation process of ideal tensile and shear strength were described in detail. Rotation angles around z, y and x for different crystal planes are listed in **Table S2**.

Table S2 Rotation angles around z, y and x for different crystal planes

Structure	Direction	Rotation angle (°)		
		α	β	γ
Diamond	Tensile			
	(100)	0	0	0
	(110)	45	0	0
	(111)	45	35.26	0
	Shear			
	$(111)[11\bar{2}]$	45	35.26	180
	$(111)[10\bar{1}]$	45	35.26	-150
Fe	Tensile			
	(100)	0	0	0
	(110)	45	0	0
	(111)	45	35.26	0
	Shear			
	(110)[001]	-45	0	-90
	$(110)[1\bar{1}0]$	-45	0	0

Calculated tensile and shear stress-strain curves for diamond and γ-Fe are shown in **Fig. S10**. From **Fig. S10 (a)**, the calculated ideal tensile strengths in the <100>, <110> and <111> directions for diamond are 205.54, 115.56 and 82.39 GPa, respectively, which indicate that the <111> direction the weakest tensile direction, and thus the (111) planes are the easy cleavage planes. The shear stress is evaluated in the easy cleavage plane (111) of diamond. The ideal shear strength in the shear directions $(111)[10\bar{1}]$ and $(111)[11\bar{2}]$ are 101.79 and 85.87 GPa, respectively. Similarly, for γ-Fe, the calculated ideal tensile strengths in the <100>, <110> and <111> directions are 52.76, 35.48 and 50.94 GPa, respectively. It indicates that the easy cleavage plane of γ-

Fe is (110). The ideal shear strength in the shear directions (111)[001] and (111)[1 $\bar{1}$0] are 38.85 and 22.19 GPa, respectively. Based on above analysis, ideal tensile and shear strength of diamond are much larger than those of γ-Fe.

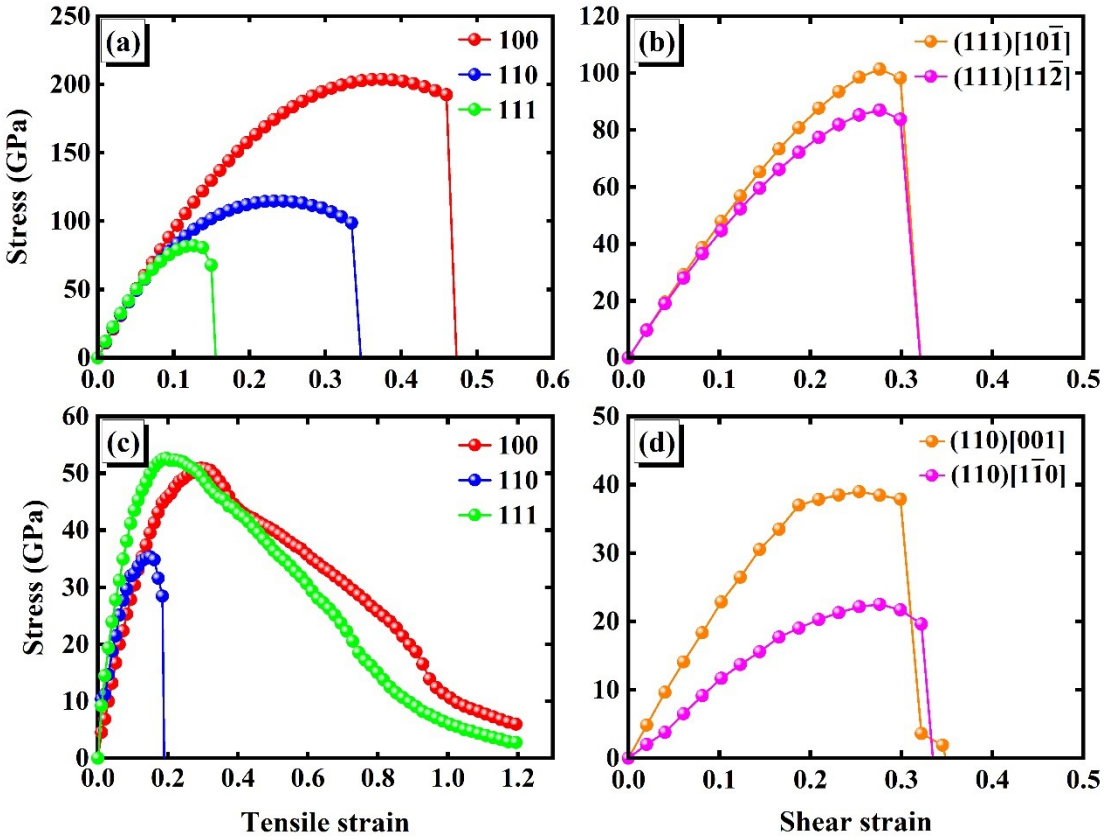

Fig. S10 Calculated tensile and shear stress-strain curves for diamond and γ-Fe. (a) and (b) are tensile and shear stress-strain curves for diamond, respectively. (c) and (d) are tensile and shear stress-strain curves for γ-Fe, respectively.

Section VI Schematic diagram of the material transfer

Figure. S11 depicts a schematic diagram of the material transfer process. Under the application of tensile stress along the Z-axis direction on the initial interface structure, as the tensile stress increases, the interface structure divides into two distinct regions, and some surface atoms from one region migrate to the other region.

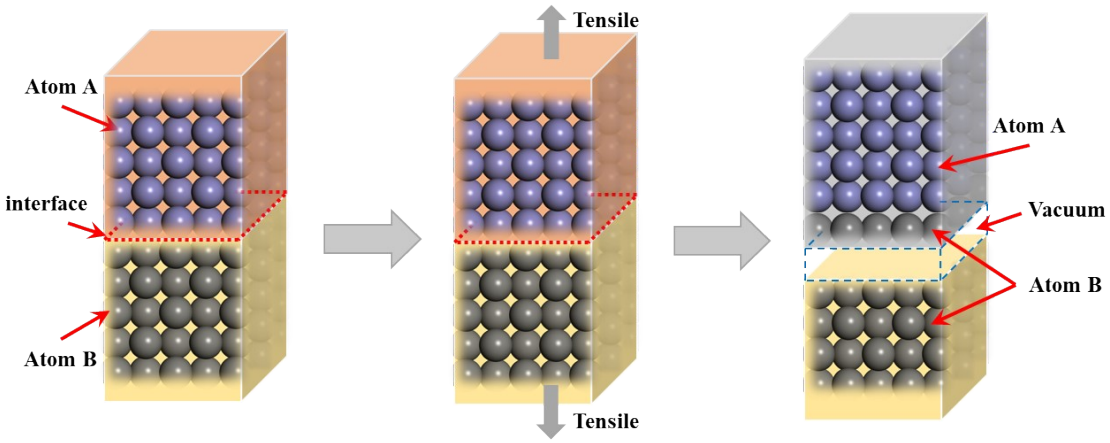

Fig. S11 Schematic diagram of the material transfer process

Reference

[1] H. Judith Grenville-Wells, K. Lonsdale, X-Ray Study of Laboratory-made Diamonds, Nature 181 (1958) 758–759. https://doi.org/10.1038/181758a0.

[2] P. Rivero, W. Shelton, V. Meunier, Surface properties of hydrogenated diamond in the presence of adsorbates: A hybrid functional DFT study, Carbon 110 (2016) 469–479. https://doi.org/10.1016/j.carbon.2016.09.050.

[3] M. Acet, H. Zähres, E.F. Wassermann, W. Pepperhoff, High-temperature moment-volume instability and anti-Invar of γ-Fe, Physical Review B 49 (1994) 6012–6017. https://doi.org/10.1103/PhysRevB.49.6012.

[4] J. Yu, X. Lin, J. Wang, J. Chen, W. Huang, First-principles study of the relaxation and energy of bcc-Fe, fcc-Fe and AISI-304 stainless steel surfaces, Applied Surface Science 255 (2009) 9032–9039. https://doi.org/10.1016/j.apsusc.2009.06.087.

[5] S. Lee, K. Esfarjani, T. Luo, J. Zhou, Z. Tian, G. Chen, Resonant bonding leads to low lattice thermal conductivity, Nature Communications 5 (2014) 3525. https://doi.org/10.1038/ncomms4525.

[6] A. D. Becke, K. E. Edgecombe, A simple measure of electron localization in atomic and molecular systems, The Journal of Chemical Physics 92 (1990) 5397. https://aip.scitation.org/doi/10.1063/1.458517.

[7] T. Lu, Q. Chen, A simple method of identifying π orbitals for non-planar systems and a protocol of studying π electronic structure, Theoretical Chemistry Accounts 139 (2020) 25. https://doi.org/10.1007/s00214-019-2541-z.

[8] Z. Liu, T. Lu, Q. Chen, An sp-hybridized all-carboatomic ring, cyclo[18]carbon: Bonding character, electron delocalization, and aromaticity, Carbon 165 (2020) 468–475. https://doi.org/10.1016/j.carbon.2020.04.099.

[9] C.D. Clark, P.J. Dean, P.V. Harris, W.C. Price, Intrinsic edge absorption in diamond, Proceedings of the Royal Society of London. Series A. Mathematical and Physical Sciences 277 (1964) 312–329. https://doi.org/10.1098/rspa.1964.0025.

[10] C.Y. Fong, B.M. Klein, Electronic and Vibrational Properties of Bulk Diamond, in: L.S. Pan, D.R. Kania (Eds.), Diamond: Electronic Properties and Applications, Springer US, Boston, MA, 1995: pp. 1–29. https://doi.org/10.1007/978-1-4615-2257-7_1.

[11] J.M. Ziman, Electrons in metals: A short guide to the Fermi surface, Contemporary Physics 4 (1962) 1–14. https://doi.org/10.1080/00107516208205824.

[12] S.B. Dugdale, Life on the edge: A beginner's guide to the Fermi surface, Physica Scripta 91 (2016) 053009. https://doi.org/10.1088/0031-8949/91/5/053009.

[13] M. Kawamura, FermiSurfer: Fermi-surface viewer providing multiple representation schemes, Computer Physics Communications 239 (2019) 197–203. https://doi.org/10.1016/j.cpc.2019.01.017.

[14] S.H. Zhang, R.F. Zhang, AELAS: Automatic ELAStic property derivations via high-throughput first-principles computation, Computer Physics Communications 220 (2017) 403–416. https://doi.org/10.1016/j.cpc.2017.07.020.

[15] R. Golesorkhtabar, P. Pavone, J. Spitaler, P. Puschnig, C. Draxl, ElaStic: A tool for calculating second-order elastic constants from first principles, Computer Physics Communications 184 (2013) 1861–1873. https://doi.org/10.1016/j.cpc.2013.03.010.

[16] F. Mouhat, F.-X. Coudert, Necessary and sufficient elastic stability conditions in various crystal systems, Physical Review B 90 (2014) 224104. https://doi.org/10.1103/PhysRevB.90.224104.

[17] W. Voigt, Lehrbuch der Kristallphysik (mit Ausschluss der Kristalloptik), Vieweg+Teubner Verlag, 1966. https://doi.org/10.1007/978-3-663-15884-4.

[18] A. Reuss, Berechnung der Fließgrenze von Mischkristallen auf Grund der Plastizitätsbedingung für Einkristalle ., ZAMM - Journal of Applied Mathematics and Mechanics / Zeitschrift Für Angewandte Mathematik Und Mechanik. 9 (1929) 49–58. https://doi.org/10.1002/zamm.19290090104.

[19] R. Hill, The Elastic Behaviour of a Crystalline Aggregate, Proceedings of the Physical Society. Section A 65 (1952) 349–354. https://doi.org/10.1088/0370-1298/65/5/307.

[20] M. Barhoumi, D. Rocca, M. Said, S. Lebègue, Elastic and mechanical properties of cubic diamond and silicon using density functional theory and the random phase approximation, Solid State Communications 324 (2021) 114136. https://doi.org/10.1016/j.ssc.2020.114136.

[21] A. Hmiel, J.M. Winey, Y.M. Gupta, M.P. Desjarlais, Nonlinear elastic response of strong solids: First-principles calculations of the third-order elastic constants of diamond, Physical Review B 93 (2016) 174113. https://doi.org/10.1103/PhysRevB.93.174113.

[22] E.S. Zouboulis, M. Grimsditch, A.K. Ramdas, S. Rodriguez, Temperature dependence of the elastic moduli of diamond: A Brillouin-scattering study, Physical Review B 57 (1998) 2889–2896. https://doi.org/10.1103/PhysRevB.57.2889.

[23] A. Migliori, H. Ledbetter, R.G. Leisure, C. Pantea, J.B. Betts, Diamond's elastic stiffnesses from 322 K to 10 K, Journal of Applied Physics 104 (2008) 053512. https://doi.org/10.1063/1.2975190.

[24] S. Fox, H.J. Jansen, Structural and magnetic properties of trigonal iron, Physical Review B 53 (1996) 5119–5122. https://doi.org/10.1103/physrevb.53.5119.

[25] B.R. Eggen, R.L. Johnston, J.N. Murrell, Carbon cluster structures and stabilities predicted from solid-state potentials, Journal of the Chemical Society, Faraday Transactions 90 (1994) 3029–3037. https://doi.org/10.1039/FT9949003029.

[26] N. Singh, Lattice Dynamics of γ-Iron at 1428 K, Physica Status Solidi (b). 156 (1989) K33–K36. https://doi.org/10.1002/pssb.2221560146.

[27] J. Zarestky, C. Stassis, Lattice dynamics of γ-Fe, Physical Review B 35 (1987) 4500–4502. https://doi.org/10.1103/PhysRevB.35.4500.

[28] S.F. Pugh, XCII. Relations between the elastic moduli and the plastic properties of polycrystalline pure metals, The London, Edinburgh, and Dublin Philosophical Magazine and Journal of Science 45 (1954) 823–843. https://doi.org/10.1080/14786440808520496.

[29] X.Q. Chen, H.Y. Niu, D.Z. Li, Y.V. Li, Modeling hardness of polycrystalline materials and bulk metallic glasses, Intermetallics 19 (2011) 1275-1281. https://doi.org/10.1016/j.intermet.2011.03.026.

[30] Y. Tian, B. Xu, Z. Zhao, Microscopic theory of hardness and design of novel superhard crystals, International Journal of Refractory Metals and Hard Materials 33 (2012) 93–106. https://doi.org/10.1016/j.ijrmhm.2012.02.021.

[31] A. Marmier, Z.A.D. Lethbridge, R.I. Walton, C.W. Smith, S.C. Parker, K.E. Evans, ElAM: A computer program for the analysis and representation of anisotropic elastic properties, Computer Physics Communications 181 (2010) 2102–2115. https://doi.org/10.1016/j.cpc.2010.08.033.

[32] S.I. Ranganathan, M. Ostoja-Starzewski, Universal Elastic Anisotropy Index, Physical Review Letters 101 (2008) 055504. https://doi.org/10.1103/PhysRevLett.101.055504.

[33] L. Rao, H. Liu, W. Shao, H. Liu, X. Xing, Y. Zhou, Z. Shi, Q. Yang, Tailoring the mechanical properties of diamond-like carbon film by doping of trace nonmetal

elements: A first-principles study, Journal of Alloys and Compounds 868 (2021) 159151. https://doi.org/10.1016/j.jallcom.2021.159151.

[34] A. Kahn, Fermi level, work function and vacuum level, Materials Horizons 3 (2015) 7–10. https://doi.org/10.1039/C5MH00160A.

[35] K. Wandelt, The local work function: Concept and implications, Applied Surface Science 111 (1997) 1–10. https://doi.org/10.1016/S0169-4332(96)00692-7.

[36] G.N. Derry, M.E. Kern, E.H. Worth, Recommended values of clean metal surface work functions, Journal of Vacuum Science & Technology A 33 (2015) 060801. https://doi.org/10.1116/1.4934685.

[37] W.A. Mackie, J.E. Plumlee, A.E. Bell, Work function measurements of diamond film surfaces, Journal of Vacuum Science & Technology B: Microelectronics and Nanometer Structures Processing, Measurement, and Phenomena 14 (1996) 2041–2045. https://doi.org/10.1116/1.588982.

[38] K.M. O'Donnell, T.L. Martin, N.A. Fox, D. Cherns, Ab initio investigation of lithium on the diamond C(100) surface, Physical Review B 82 (2010) 115303. https://doi.org/10.1103/PhysRevB.82.115303.

[39] van der Weide J., Z. Zhang, P.K. Baumann, M.G. Wensell, J. Bernholc, R.J. Nemanich, Negative-electron-affinity effects on the diamond (100) surface, Physical Review B 50 (1994) 5803–5806. https://doi.org/10.1103/physrevb.50.5803.